Network structure and dynamics of effective models of nonequilibrium quantum transport

Abigail N. Poteshman [1,*] Mathieu Ouellet [2] Lee C. Bassett,[2,†] and Dani S. Bassett [1,2,3,4,†]

[1]*Department of Physics & Astronomy, College of Arts & Sciences, University of Pennsylvania, Philadelphia, Pennsylvania 19104, USA*

[2]*Department of Electrical & Systems Engineering, School of Engineering & Applied Science, University of Pennsylvania, Philadelphia, Pennsylvania 19104, USA*

[3]*Department of Bioengineering, School of Engineering & Applied Science, University of Pennsylvania, Philadelphia, Pennsylvania 19104, USA*

[4]*Santa Fe Institute, Santa Fe, New Mexico 87501, USA*

Across all scales of the physical world, dynamical systems can be usefully represented as abstract networks that encode the systems' units and interunit interactions. Understanding how physical rules shape the topological structure of those networks can clarify a system's function and enhance our ability to design, guide, or control its behavior. In the emerging area of quantum network science, a key challenge lies in distinguishing between the topological properties that reflect a system's underlying physics and those that reflect the assumptions of the employed conceptual model. To elucidate and address this challenge, we study networks that represent nonequilibrium quantum-electronic transport through quantum antidot devices—an example of an open, mesoscopic quantum system. The network representations correspond to two different models of internal antidot states: a single-particle, noninteracting model and an effective model for collective excitations including Coulomb interactions. In these networks, nodes represent accessible energy states and edges represent allowed transitions. We find that both models reflect spin conservation rules in the network topology through bipartiteness and the presence of only even-length cycles. The models diverge, however, in the minimum length of cycle basis elements, in a manner that depends on whether electrons are considered to be distinguishable. Furthermore, the two models reflect spin-conserving relaxation effects differently, as evident in both the degree distribution and the cycle-basis length distribution. Collectively, these observations serve to elucidate the relationship between network structure and physical constraints in quantum-mechanical models. More generally, our approach underscores the utility of network science in understanding the dynamics of quantum systems.

I. INTRODUCTION

The intersection of network science and quantum physics is an emerging area of interdisciplinary research [1,2]. Methods from network science have been used to characterize features of quantum networks that are relevant to the design of quantum information and communication systems, such as quantum synchronization [3], transport efficiency [4], and robustness to noise [5]. Conversely, quantum effects and dynamics have been applied to complex networks, such as by modeling quantum walks [6,7], partitioning networks [8,9], and representing nodes as entangled states [10]. In both directions of inquiry, interdisciplinary work has focused

on manipulating network structure to optimize networks for quantum information processing, storage, and communication technologies. Yet, this focus has necessarily neglected the important space of questions surrounding how network structure emerges naturally and directly from quantum systems themselves. In previous work, we sought to address this gap by considering the structure of mesoscopic quantum networks, and by demonstrating the utility of network characterizations in explaining transport properties [11]. Here we take a complementary approach and ask: What network topology emerges from different physical models of mesoscopic quantum systems? And how are these differences in network topology impacted by underlying system dynamics?

Mesoscopic quantum systems, such as quantum dots and quantum antidots, are of particular interest to those designing quantum information processing devices [12–15]. They are widely tunable and can be efficiently controlled electronically by capacitive coupling to electrostatic gates that can alter their equilibrium charge [16–19]. Mesoscopic quantum systems can be probed with transport experiments: electrons tunneling between reservoirs weakly coupled to a mesoscopic system induce transitions between quantum mechanical configurations, whose properties can be deduced from measurements of current and conductance. Features of mesoscopic systems, however, are difficult to characterize and predict since

*Present address: Committee on Computational and Applied Mathematics, Physical Sciences Division, University of Chicago, Chicago, Illinois 60637, USA.

†These authors contributed equally; lbassett@seas.upenn.edu and dsb@seas.upenn.edu
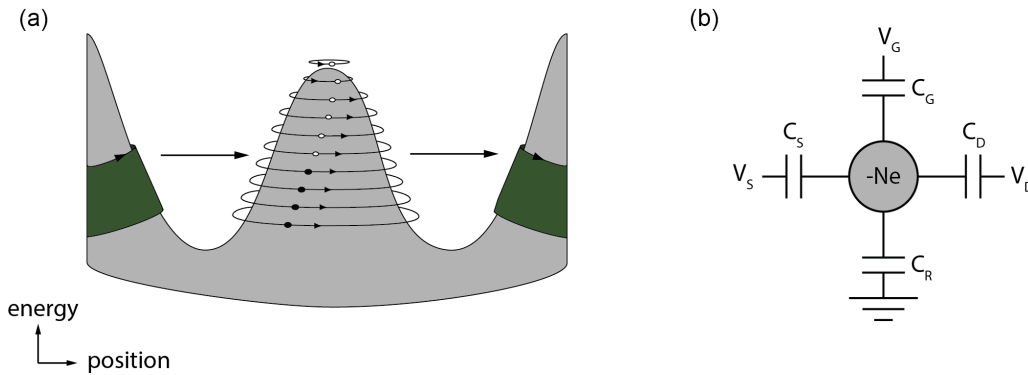
FIG. 1. An overview of antidot physics. (a) Schematic cross section of an antidot. Tunneling occurs between edge states carrying a Fermi sea of electrons (green) and quantized antidot energy states. (b) Equivalent capacitor network for the antidot electrostatics. The quantized charge on the antidot is $-Ne$, where N is the number of electrons (relative to a fixed reference configuration) and e is the electron charge. The electrostatic potential of the antidot is controlled *via* capacitive couplings (C_S, C_D, C_G) to the source, drain, and gate voltages (V_S, V_D, V_G). Any remaining coupling to other elements of the device is modeled as a capacitive coupling to the ground potential (C_R), such that the total capacitance is $C = C_S + C_D + C_G + C_R$. Figure adapted from Ref. [31].

simulating a many-body interacting system is computationally intractable due to exponential scaling of the system's Hilbert space with particle number [20,21]. Without true quantum simulators, the best tools available to model mesoscopic systems are numerical, semiclassical models.

In the recent literature, network science has emerged as a promising tool to offer intuition for the architectures of physical systems that produce mesoscopic dynamics [22–26]. Network science provides a complementary tool to elucidate emergent properties of interacting systems rather than a computational shortcut to calculate the same properties one arrives at directly from the underlying models used to construct the networks. For example, in a previous study employing a single-particle model of quantum-electronic transport, we demonstrated that statistical characterizations from network science can capture physically-relevant emergent properties of nonequilibrium transport [11]. Yet, the work left unanswered the question of how different physical constraints embedded in various models of quantum phenomena are reflected in the network architecture [27,28]. That such reflections might exist is intuitively plausible when one considers the nature of the physical models, which can represent quantum states and mechanisms for state excitation quite differently, for example, by using different bases or at different levels of approximation [29,30].

To better understand the interdigitation between physics and topology, we study networks constructed from two models of nonequilibrium transport through a quantum antidot [see Fig. 1(a)]: a single-particle model and an effective model [31]. Both models produce experimentally accurate time-averaged values of current and conductance from transport experiments, but describe the internal antidot configurations and mechanisms for excitations in different ways [31]. The single-particle model treats quantum states as composed of distinguishable, noninteracting elementary particles, whereas the interacting model describes quantum states in terms of collective quasiparticle excitations of a many-body liquid. That is, the two models are not merely different basis representations of the same physics. We performed a statistical investigation of the models' network topology, paying

particular attention to the network's cycle structure and degree distribution, which are high-order and lower-order, respectively, topological characteristics relevant to the propagation of information and control profiles of complex networks [32–34].The framework of network construction and topological analysis enables a systematic study of the differences between the single-particle and effective models, since these subtleties are not captured by the static, time-averaged experiments measuring current and conductance. By characterizing networks built from these two models, we demonstrate that the physical constraints and dynamics encoded in different effective models manifest in their network topology. While outside the scope of this paper, our approach paves the way for future studies on the control profiles of quantum networks, with implications for devising specific quantum control strategies.

II. METHODS

Here, we extend previous work that built a network model of the energy landscape of nonequilibrium transport through quantum antidots [11]. Expanding upon that study, we now consider an effective model in addition to a single-particle model of antidot states. We also examine the impact of including spin-conserving relaxation effects on network structure. Together, these extensions allow us to ask (and answer) further questions about the relations between physical processes and resultant network topology in mesoscopic quantum systems.

A. Transport regime of interest

For an overview of transport through mesoscopic systems, and antidots in particular, we direct readers to seminal reviews such as Refs. [16–19]. Here, we focus on spin-resolved transport through a single quantum antidot at filling factor $\nu_{AD} = 2$ in the integer quantum Hall regime at relatively low magnetic fields ($B < 1$ T) see Fig. 1(a). In this regime, both the single-particle and effective models of internal antidot configurations qualitatively describe transport experiments [35,36]. For further details on nonequilibrium transport through

quantum antidots in this particular regime, we direct readers to Refs. [11,31].

To quantitatively characterize transport in an antidot system weakly coupled to extended metallic leads, experiments measure (and models predict) the current, I, and the differential conductance, $G = \frac{dI}{dV}$. Nonzero current indicates the presence of accessible quantum states in the antidot within the energy window defined by the relative electrochemical potentials of the source, μ_S, and drain, μ_D [see Fig. 1(b)]. Differential conductance reflects changes in the transport configurations, generally due to changes in the alignment of state transitions with μ_S and μ_D. Differential conductance is typically positive but can become negative in certain configurations. Together, current and conductance are used as both qualitative and quantitative indicators of quantum transport phenomena, and they are the key output of computational models for comparison with experiments [11,31].

The number of relevant antidot states involved with nonequilibrium quantum transport grows rapidly with the applied bias [see Fig. 1(b)]. The additional states relevant for nonequilibrium transport include excited states that represent different spin and orbital configurations [18]. The ways in which these spin and orbital configurations are connected through tunneling and relaxation events are manifold, leading to a richly structured collective energy landscape. In fact, landscape complexity grows exponentially with particle number; it quickly becomes computationally intractable to calculate transport characteristics analytically. As a result, the best tools available to model nonequilibrium transport through mesoscopic systems are numerical, semiclassical models. Quantum antidot states can be modeled either in terms of the electron state occupation number (see Sec. II B) or as edge waves in the charge distribution (see Sec. II C) [36]. In the open geometry of an antidot, the number of electrons associated with a particular energy state is undefined; instead, we employ a particle-hole transformation to describe the system in terms of a finite number of holes [31].

B. Single-particle model

Here we provide a brief description of the single-particle model for transport through quantum antidots (see Ref. [11] for further details). The single-particle energies are labeled by orbital ($m = 0, 1, 2, \ldots$) and spin ($\sigma = \pm \frac{1}{2}$) quantum numbers,

$$\varepsilon_{m\sigma} = m\Delta E_{\mathrm{SP}} + \sigma E_{\mathrm{Z}}, \qquad (1)$$

yielding an energy spectrum of two ladders of equally spaced energy levels. The spacing between orbital energy levels, ΔE_{SP}, is assumed to be constant, and the separation between energy ladders is the Zeeman energy E_{Z}. Excitations are also governed by these two energy scales, with possible values

$$E_{\mathrm{ex}} = j\Delta E_{\mathrm{SP}} \pm q E_{\mathrm{Z}}, \qquad (2)$$

where $q = 0$ and $q = 1$ represent spin-conserving or spin-flip transitions, respectively, and j is any integer. Internal quantum states of the antidot are represented as a pair of electronic occupation vectors $(\mathbf{n}_\uparrow, \mathbf{n}_\downarrow)$, with components $n_{m\sigma} = 0$ or 1 for each orbital, m, and spin, σ. Since we can track whether electrons occupy specific orbitals, the electrons in the

single-particle model are distinguishable. Once the possible electronic occupation vectors are enumerated, a Boolean set of selection rules can be calculated by determining which sets of electronic occupation vectors differ by exactly one electron. That is, if the XOR sum of two sets of electronic occupation vectors is exactly 1, then the transition is allowed. Otherwise, the transition is forbidden.

C. Effective model

We can also consider an effective model of antidot states, in which electrons are indistinguishable and excited states are described as collective excitations of a quantum liquid around the antidot edge [36,37]. The effective model is based on the full Hamiltonian for a system of N interacting electrons within the standard Born-Oppenheimer approximation in which the electronic degrees of freedom are decoupled from those of the lattice [38]. The Hamiltonian can be written in the form

$$\hat{H} = \sum_i^N \hat{h}_i + \frac{e^2}{4\pi\epsilon\epsilon_0} \sum_{i>j}^N \frac{1}{|\mathbf{x}_i - \mathbf{x}_j|}, \qquad (3)$$

where $\hat{h}_i$ is the single-particle Hamiltonian acting on the ith electron, which is given by

$$\hat{h}_i = \frac{1}{2m^*}(-i\hbar\boldsymbol{\nabla}_i + e\mathbf{A})^2 - e\varphi(\mathbf{x}_i) - g\mu_{\mathrm{B}}B\hat{s}_{zi}. \qquad (4)$$

This general Hamiltonian does not have any known analytic solutions for more than one electron.

Using Hartree-Fock mean-field theory (see Sec. I A of the Supplemental Material [39]), we assume that each electron in the multielectron system is described by its own single-particle wave function [Eq. (4)]. The multielectron wave function Ψ can be written as a Slater determinant of orthonomal single-particle spin orbitals, and we can obtain the total energy E for Ψ using the variational principle [31]. In this way, we obtain a fermionic basis of multiparticle states, which characterizes antidot states by occupation numbers of fermion orbitals. Since the fermionic basis states are not general eigenstates of the interacting Hamiltonian [Eq. (3)], we obtained the eigenenergies by diagonalizing the matrix Hamiltonian constructed from the subspace of fermionic basis states with a given (M, S_z), using the rules for addition of angular momentum [36]. This process leads to a bosonic basis, in which the neutral excitations are described by a spectrum of edge waves similar to the one-dimensional Tomonaga-Luttinger liquid model [40,41].

The antidot states and transition rules among them are defined as follows. In the effective model, the antidot states are given by $|N, S_Z, n_L, n_S\rangle$, where N is the particle number of the state, S_Z is the total spin projection, $n_L \in \mathbb{Z}^+$ is the excitation of the density modes, and $n_S \in \mathbb{Z}^+$ is the excitation of the spin modes. The ground-state configurations, $|N, S_z, 0, 0\rangle$, are known as maximum density droplets [37]. For these configurations, the fermionic basis states remain eigenstates of the interacting Hamiltonian and we can accurately calculate their energies using Hartree-Fock theory. For consistency between the single-particle and effective models, we use the same ground-state energy calculations in both simulations. The configuration energy for an arbitrary state in the effective model is
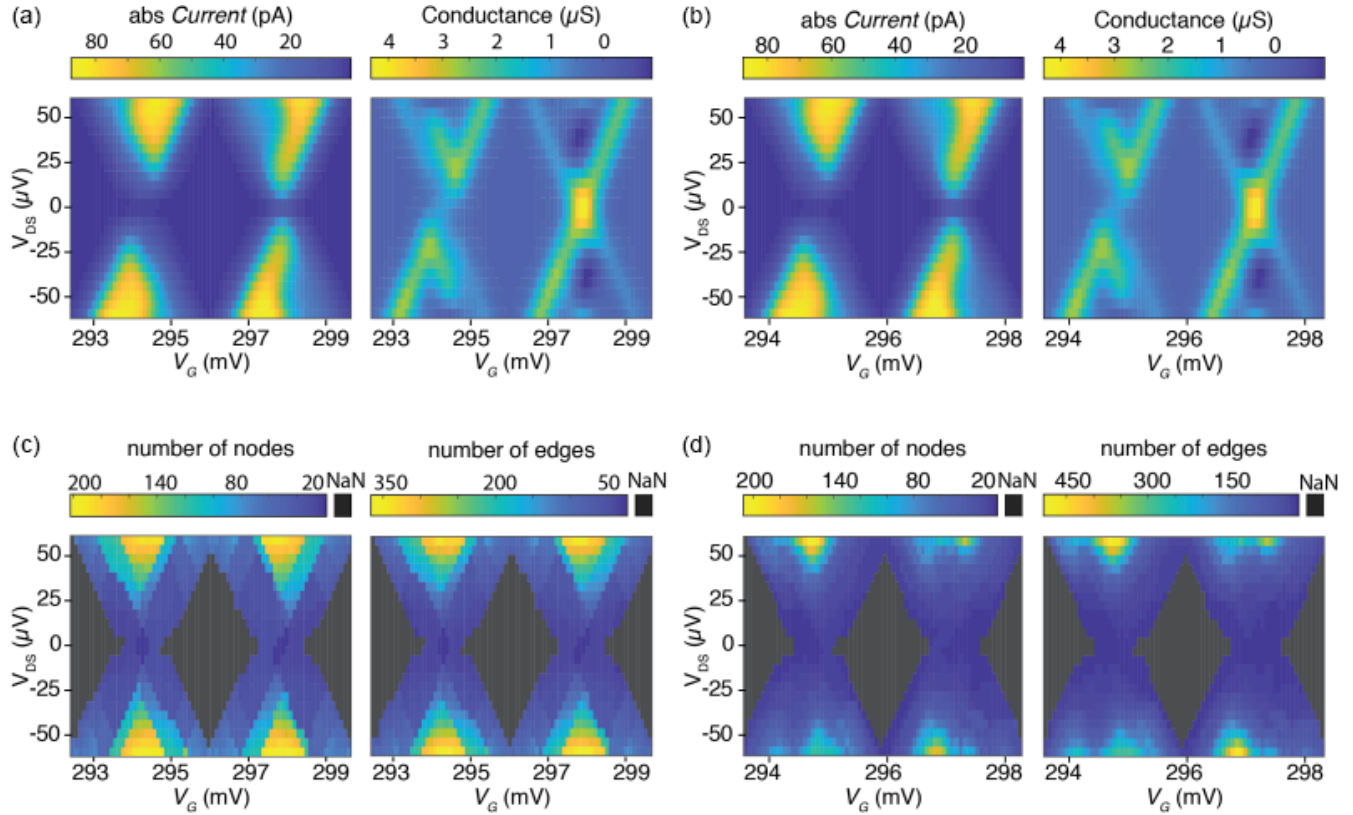
FIG. 2. Single-particle model versus effective model of nonequilibrium transport through quantum antidots. Current and conductance calculations based on a single-particle model (a) and an effective model (b) of energy states in quantum antidots. Both models were run with the following parameters: T = 50 mK, **B** = 1.2 T, effective spin-up tunneling rate $\Gamma_\uparrow = 500$ MHz, and effective spin-down tunneling rate $\Gamma_\downarrow = 50$ MHz. All subsequent figures are based on models run with these parameters unless noted otherwise. The number of nodes and the number of edges for the networks corresponding to each set of voltage settings constructed based on a single-particle model (c) and an effective model (d) of energy states. Note that we excluded networks corresponding to voltage settings that result in a current with magnitude less than 1 pA from our analysis; the values in panels (c) and (d) that are displayed as NaN indicate that networks were excluded.

given by $U(|N, S_Z, n_L, n_S\rangle) = U(|N, S_Z, 0, 0\rangle) + n_L \times E_L + n_S \times E_S$, where E_L is the energy scale for the density mode excitations and E_S is the energy scale for the spin-mode excitations. A transition between two states of the effective model is allowed if $\Delta N = \pm 1$ and $\Delta n_S \in \{\frac{1}{2}, -\frac{1}{2}\} - \Delta|S_Z|$. The binary selection rules are weighted by the Clebsch Gordan coefficient for the addition of the spins S_Z and $S_Z \pm \frac{1}{2}$ corresponding to the transition. This model of weighted selection rules qualitatively replicates asymmetries in the conductance map over the voltage space [see Fig. 2(b)] observed in experiments [31].

D. Computational model of transport through a quantum antidot

The physics of the antidot enters the calculation in the form of a set of quantum states, its associated energy spectrum, and a set of matrix elements for transitions between states. However, the method to construct and solve a dynamical transition-rate matrix for the steady-state probabilities of the antidot is agnostic to the physical model used to obtain the quantum states. We used the same dynamical rate-equation approach to obtain steady-state probability occupations for the antidot's configurations as in Ref. [11].

In Secs. II B and II C, we described two different models of internal antidot configurations, which yield different descriptions of the quantum states and transition rules. In both cases, however, the total particle number, N, and the spin projection, S_z, are good quantum numbers, and hence the selection rules between quantum states can be written in block-matrix form, e.g.,

$$
\begin{pmatrix}
0 & W^{+\downarrow}_{S_{z0}-1} & & & \cdots & & 0 \\
W^{-\downarrow}_{S_{z0}-\frac{3}{2}} & 0 & W^{-\uparrow}_{S_{z0}-\frac{1}{2}} & & & & \vdots \\
& W^{+\uparrow}_{S_{z0}-1} & 0 & W^{+\downarrow}_{S_{z0}} & & & \\
& & W^{-\downarrow}_{S_{z0}-\frac{1}{2}} & 0 & W^{-\uparrow}_{S_{z0}+\frac{1}{2}} & & \\
\vdots & & & W^{+\uparrow}_{S_{z0}} & 0 & W^{+\downarrow}_{S_{z0}+1} \\
0 & & \cdots & & W^{-\downarrow}_{S_{z0}+\frac{1}{2}} & 0
\end{pmatrix}.
$$

(5)

Here, the states are organized as groups that define each block, $\{|N, S_z\rangle\}$, with S_z increasing from top to bottom (S_{z0} is the ground-state spin projection) and N alternating between two adjacent integer values. The submatrices $W^{\pm\sigma}_{S_z}$ contain the selection rules for adding (+) or removing (−) a particle of spin σ to a state with initial spin projection S_z. The specific states included in the model (both the number of

blocks and the number of states in each block) are determined through energy and dynamical considerations for a given bias configuration.

The transition rates $\gamma_{s' \to s}$ from antidot configuration $|s'\rangle$ to $|s\rangle$ are calculated according to a combination of antidot selection rules and Fermi's golden rule (see Sec. I B of the Supplemental Material for a full derivation of the transition rates). The resulting transition rate matrix, **R**, is defined by $R_{ij} = \gamma_{s_i s_j} = \gamma_{s_j \to s_i}$, where i and j represent different configurations. We seek the steady-state configuration where the total transition rate into and out of each state is equal, and the solution to the dynamical rate equation yields the steady-state occupation probabilities **P** (see Refs. [11,31] for details about the dynamical rate-equation approach). From **P**, we can compute the current flowing from each spin-polarized reservoir and the spin-resolved conductance [31].

Using this computational model, we can simulate quantum transport as a function of experimental parameter settings including gate voltages, drain-source bias, magnetic field, and temperature, and we can choose whether to use an energy spectrum based on a single-particle model or an effective model. Figures 2(a) and 2(b), respectively, show transport simulations for the single-particle and effective models. The settings chosen in this paper are motivated by spin-resolved transport experiments in which the underlying physical parameters (e.g., ΔE_{SP}, E_Z, and the spin-dependent tunneling rates) have been well characterized [31]. Unless indicated otherwise, the temperature is 50 mK, $\Delta E_{\mathrm{SP}} = 30.7\,\mu\mathrm{eV}$, $E_Z = 45.8\,\mu\mathrm{eV}$, $E_C = 85\,\mu\mathrm{eV}$, the effective spin-up tunneling rate is 500 MHz, and the effective spin-down tunneling rate is 50 MHz. For details on how the experimental parameter settings enter into quantum transport calculations, see Secs. I B–I D of the Supplemental Material. For a direct comparison of the qualitative agreement between experimental measurements and calculations based on the single-particle and effective models, see Sec. I E of the Supplemental Material.

E. Spin-conserving relaxation effects

We can include spin-conserving relaxation effects within each set of antidot configurations with the same number of particles and total spin $\{|N, S_z|\}$ by adding block matrices **T** describing these processes to the main diagonal of the matrix in Eq. (5) [31]. For the single-particle model, we encoded the spin-conserving relaxations as $T_{ij} = 1$ if state j results from moving one of the electrons in state i to the lowest available orbital in state i, and $T_{ij} = 0$ otherwise. For the effective model, we set $T_{ij} = 1$ if state i (represented as $|N_i, S_{Zi}, n_{Li}, n_{Si}\rangle$) and state j (represented as $|N_j, S_{Zj}, n_{Lj}, n_{Sj}\rangle$) have the same total spin ($N_i = N_j$) and spin-mode excitation ($n_{Si} = n_{Sj}$), and state i is a density mode excitation of state j ($n_{Lj} < n_{Li}$). For both models, the relaxation rate was set at 500 MHz when relaxation was included, which is on the same order as the tunneling rates into and out of the antidot.

F. Dynamical properties and null models

To investigate dynamical differences between the models, we explored how a random walker would move in the state space. To do so, we considered the rate matrices **R** of both models and used the steady-state occupation probability **P** to weight the probability of selecting an initial position [see Figs. 3(a) and 3(b)]. We initialized 10 000 random walkers and evolved the system forward for 10 000 time steps. We characterize the dynamics quantitatively by the degree of diffusion, defined as the length of the shortest transition path from the walker's initial starting point to its current point.

To investigate how the dynamics of the models, as defined by the steady-state occupation probabilities **P** combined with transition rate matrices **R**, drive network topology, we perform a null model analysis of the average dynamical cycle length for random walkers in the state space. The average dynamical cycle length is defined as the average of the distance a walker travels before returning to a specific node. For the null models, we test the impacts of initializing the random walkers with uniform probability, evolving the walkers based on an unweighted transition matrix, and evolving the walkers based on weighted transition matrices wherein the weights are shuffled among existing edges. These sets of experiments preserve the network connectivity but alter the dynamics of the evolution.

G. Network construction and statistical characterization

Similar to constructing a dynamical equation that determines the transition rate matrix and the occupation probabilities, the method to construct networks is agnostic to the underlying physical model used to represent antidot configurations. In the networks representing transport through quantum antidots, the nodes represent antidot configurations and the edges represent possible transitions between configurations after single electron tunneling events and relaxation events. We used the same method to construct networks based on the transition rate matrices **R** [see Figs. 4(a) and 4(b) and Supplemental Material Figs. S5(a) and S5(b)] and corresponding probability vectors **P** as reported in Ref. [11]. The thresholding method for the probability vectors is presented in Sec. I F of the Supplemental Material.

With these adjacency matrix representations of our network in hand, we can begin to perform rigorous statistical characterizations of network size, density, and topology [42]. The number of nodes n in a network is given by the size of the matrix, and the number of edges in the network is the number of nonzero elements in the matrix [see Figs. 2(c) and 2(d) and Supplemental Material Figs. S4(c) and S4(d)]. To evaluate the network's topology, we focus on two statistical measures relevant to a network's capacity to propagate current, signals, nutrients, or other physical, biological, or informational items [32,33]: the network's degree distribution and cycle structure. The degree of a node i is the sum over i of A_{ij}. A narrow degree distribution is indicative of a particularly ordered systems; in a lattice, for example, the degree distribution is a delta function because every node has the same degree, given by the number of its immediately adjacent neighbors [43]. A broad degree distribution is indicative of more complexity, where some parts of the system are heavily connected (forming network hubs), and other parts of the system are less connected [44]. In fact, degree heterogeneity is a direct quantification of a network's complexity as formalized in the notion of entropy [45].
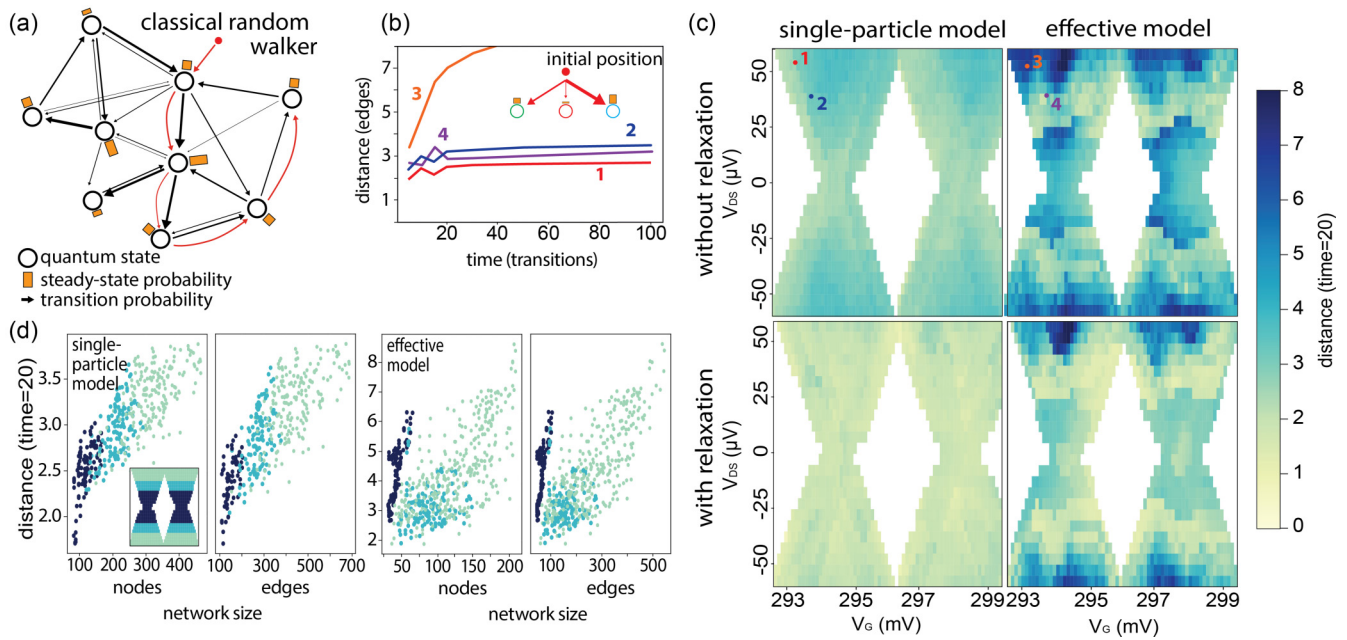
FIG. 3. Random walk dynamics on the state space. (a) A classical random walker starts in a random state in the state space and transitions on the graph following the rate matrix **R**. (b) The distance of the random walker as a function of time. Distance is measured in terms of the length of the shortest transition path from the walker's initial starting point to its current point. Here we show the distance for the system's parameter values shown in (c). (c) The distance from the initial starting point at $t = 20$ for the single-particle and the effective model, both with and without relaxation. A shortest transition path is calculated for each of 10 000 random walkers; here we plot the average over those 10 000 simulations. The initial starting point of the random walker is weighted by the steady-state probability obtained in the steady-state analysis. (d) The number of nodes and the number of edges for the physical conditions of panel (c), separately plotted for the single-particle and effective models. Color indicates V_{DS}.

The distribution of node degrees is a so-called *lower-order* topological characteristic that considers only the edges in a node's immediate neighborhood: those edges that connect the node directly to other nodes. Ongoing work in the field of network science, however, continues to demonstrate that *higher-order* topological characteristics—those that characterize the organization of edges which are more than 1 hop away from a node—have important roles to play in system dynamics and control [45–49]. It therefore seems prudent to consider both lower-order and higher-order topological statistics in our evaluation. In choosing each, we considered the growing body of evidence indicating that degree distribution (lower-order) and cycle structure (higher-order) are two specific network features that consistently shape the dynamics, capacity for information storage, and control profile of a network [32,44,50–52]. We therefore complemented the examination of the degree distribution with an examination of the network's cycle basis, which can be algorithmically extracted using the python software package NETWORKX [53,54].
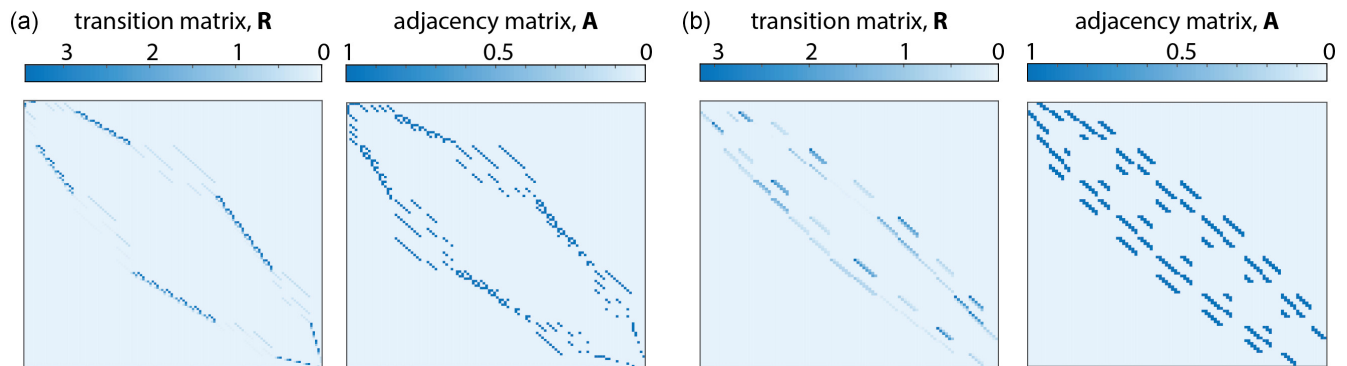

FIG. 4. Example rate and adjacency matrices. (a) Example transition rate matrix **R** (left) and its corresponding adjacency matrix **A** (right) obtained using a single-particle model of quantum transport. The network these matrices represent corresponds to voltage settings resulting in a current of $|I| = 81.0$ pA and 112 states. (b) Example transition rate matrix **R** (left) and its corresponding adjacency matrix **A** (right) obtained using an effective model of quantum transport. The network these matrices represent corresponds to voltage settings resulting in a current of $|I| = 81.8$ pA and 98 states.

A cycle is a closed walk that does not retrace any edges immediately after traversing them. Cycles are particularly relevant for understanding transport because a dense cycle structure has been shown to be optimal for transport in the face of spatially and temporally varying loads [55] and to provide resilience of transport following network damage [56]. A cycle basis is a basis for the vector space of all cycles, defined over $\mathbb{Z}_2$, such that all cycles of a network can be expressed in terms of linear combinations of elements in the cycle basis. Although a network can be decomposed into a cycle basis in many different ways, the length distribution of the cycle basis elements is unique [57]. Since extracting the cycle basis of a network can be computed in polynomial time, in contrast with an exhaustive enumeration of all possible cycles which requires exponential time, our analysis of cycle structure is restricted to considering the length of cycle basis elements in this paper [58], an approach similar to one recently used for characterizing hydrogen bond network topology [59]. Together, the degree distribution and cycle basis allow us to examine the interplay between network topology and mesoscopic physics.

III. RESULTS

By examining networks constructed from two models of nonequilibrium transport through quantum antidots, we can explore which aspects of energy-state transition networks are common to the physical process of transport versus which aspects reflect particular transport mechanisms. The former will manifest as characteristics common to all transport networks, and the latter will manifest as characteristics that vary across transport models. We begin by examining dynamical differences between the two models of antidot transport.

A. Dynamical properties of the transition rate matrices

Both models give similar quantitative and qualitative results for the steady-state properties of the system in the desired experimental parameter range. Yet, this fact does not require the time evolution of the two models to be equivalent. To investigate dynamical differences between the models, we explored how a random walker would move in the state space. To do so, we considered the rate matrices **R** of both models and used the steady-state occupation probability to weight the probability of selecting an initial position [see Figs. 3(a) and 3(b)]. The two models display markedly different patterns of distance from their initial position after 20 steps [see Fig. 3(c)]. Here we quantify these differences in terms of the degree of diffusion and in terms of the continuity of distance as a function of applied bias. We will consider the latter first.

The single-particle model displays a continuous transition among distances for all values of V_G when varying the bias potential V_{DS}. In contrast, the effective model displays a notable discontinuity for moderate bias going from a distance of more than six edges to a distance of less than three edges within a few microvolts. The presence of a discontinuity in the effective model can be further appreciated when considering basic network metrics like the number of nodes or the number of edges for the physical graph. The single-particle model displays a smooth transition in these two metrics for the full range of V_{DS} [see Fig. 3(d)]. In contrast, the effective model

displays a discontinuous transition in these two metrics as V_{DS} enters and exits the middling range (colored navy blue in the figure).

To complement our examination of the continuity or discontinuity in distance as a function of V_{DS}, we study the extent of diffusion in each model. The single-particle model displays a consistently low amount of diffusion, a distance of around three edges, regardless of network size or location in voltage space. In contrast, the effective model displays diffusive behavior that varies dramatically and discontinuously across regions within the voltage space, from a distance of eight edges in some regions to a distance of one in others [see Fig. 3(c)]. That is, the effective model displays regions of both much greater and much lower diffusion compared to the single-particle model. Since the qualitative diffusion properties vary across these two underlying physical models, and these qualitative differences are not a direct reflection of network size, a deeper analysis of the topology is needed to understand the interplay between physical rules, network topology, and dynamical properties. The following sections tackle this question by modeling the transition network as a general graph and examining both higher- and lower-order topological characteristics, and then we turn back to examine the ways in which the transport dynamics themselves drive these topological characteristics.

B. Spin constraints lead to bipartite networks

Using two models of non-equilibrium transport through quantum antidots—a single-particle model and an effective model—we constructed networks over a range of voltage configurations spanning two Coulomb diamonds [see Figs. 2(a) and 2(b)]. Transport calculations using both models agree with experimental values of current and conductance [see Figs. 2(c) and 2(d)], but the models assume quite different transport mechanisms. We first examined networks constructed from both models when excluding relaxation effects. We found that all networks from both models are bipartite. A bipartite network has two classes of nodes and edges that connect only nodes of one class with nodes of the other class [60]. Intuitively then, bipartiteness reflects the shared spin conservation rules that are a common underlying constraint upon both models. Edges represent single tunneling events of electrons into or out of the antidot, so neighboring nodes differ by $\frac{1}{2}$ total spin [see Fig. 5(a)]. Understanding edges as single-electron tunneling events leads to a natural two-color marking scheme of integer versus half-integer total spins [Fig. 5(b)].

As a direct extension of their bipartite nature, we found that all networks contained only even-length cycles in their cycle bases [see Figs. 5(c) and 5(d)]. Recall that a cycle is a closed walk that does not retrace any edges immediately after traversing them. To complete a cycle and return to the starting antidot configuration (node), an even number of tunneling events must occur since each tunneling event (edge) changes the total spin of a state (node) by $\frac{1}{2}$. While networks constructed using an effective model have a minimum cycle length of 4 in their cycle bases elements—an expected minimum length since in the network representations, a 2-cycle is simply an edge—networks constructed using the single-particle model have a minimum cycle length of 6 [see Fig. 5(d)].
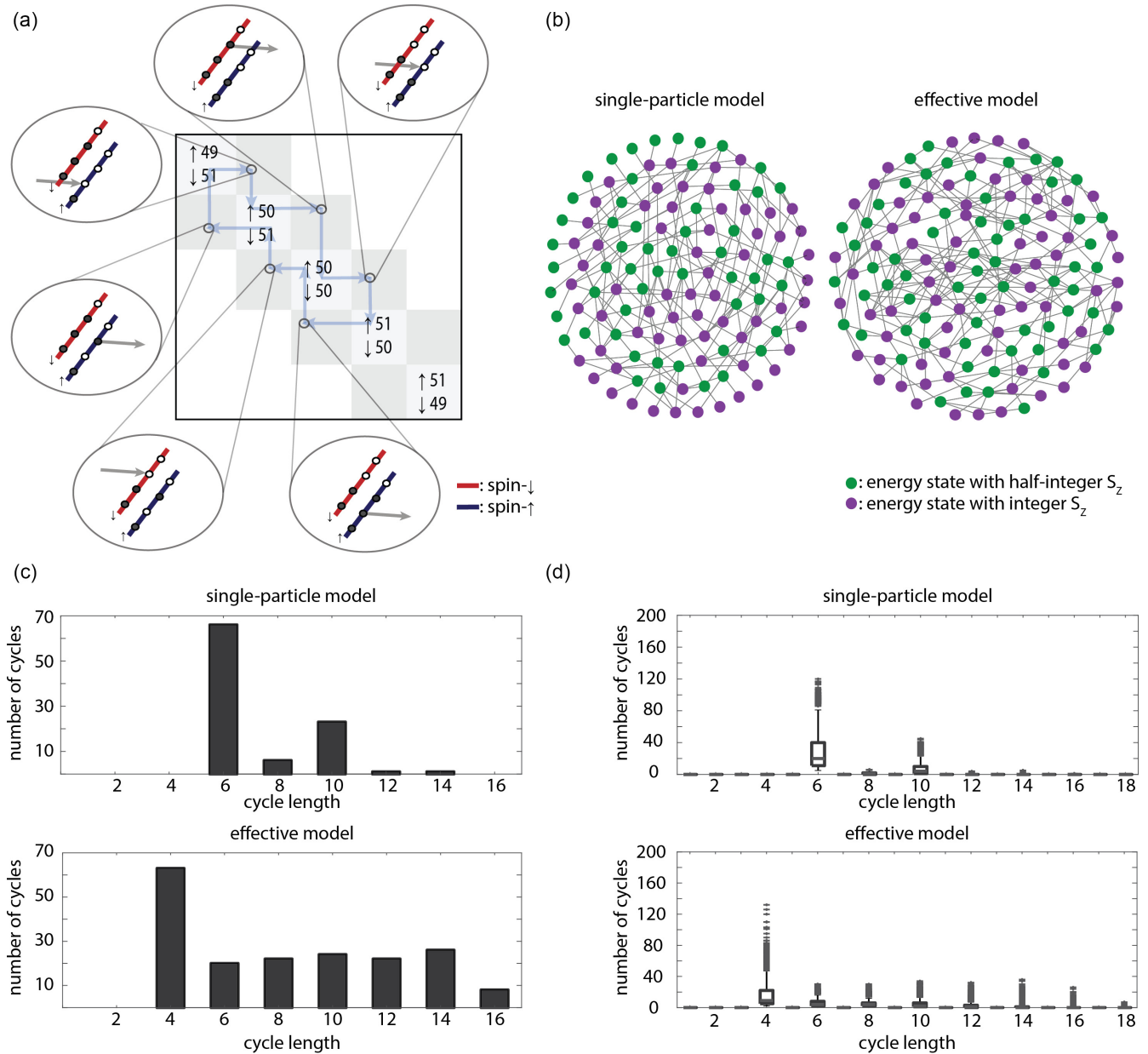
FIG. 5. Spin constraints result in even-length cycles. (a) A schematic of cycle trajectory through an adjacency matrix representation of a network. The block diagonal represents antidot energy-state configurations that the system may occupy, and the grey off-diagonal blocks store transition rates between antidot states. The cycle shown in the schematic corresponds to a cycle of length 6, where each node in the cycle is a distinct antidot configuration in the diagonal block, and each edge is represented by two blue arrows that pass from one node through a transition rate to a new node. Spin-preserving relaxations occur within a diagonal block. Since the schematic shows an implementation of transport without relaxation, the system must pass through a grey transition state to move from one node to another. Since the spin changes by a half-integer amount during each transition, all cycles have an even length. (b) Sample networks with a two-coloring scheme, where nodes having an integer spin are shown in purple and nodes having a half-integer spin are shown in green for a single particle noninteracting model (left) and for an effective model (right). (c) Distribution of cycle length in the cycle basis space for the single networks shown in (b). (d) Distribution of cycle lengths for all networks over the voltage space displayed in Fig. 2 corresponding to a current greater than 1 pA for the networks constructed from the single-particle model (top) and from the effective model (bottom). In each box plot, the central mark represents the median, the top and bottom edges indicate the third and first quartiles, the whiskers extend to $\pm 2.7\sigma$, and individual outliers are displayed by $-$.

The difference in minimum cycle lengths stems from a fundamental difference between the single-particle model and the effective model. In the single-particle model, particles are distinguishable, and individual electrons occupy specific excited states. In the effective model, particles are indistinguishable, and excitations of density and spin modes are represented collectively. Enumerating all of the possible 4-cycles, we observe two constraints that prohibit these cycles from occurring for the single-particle model [see Fig. 6(a)], but there exist 6-cycles for the single-particle model that do not violate these
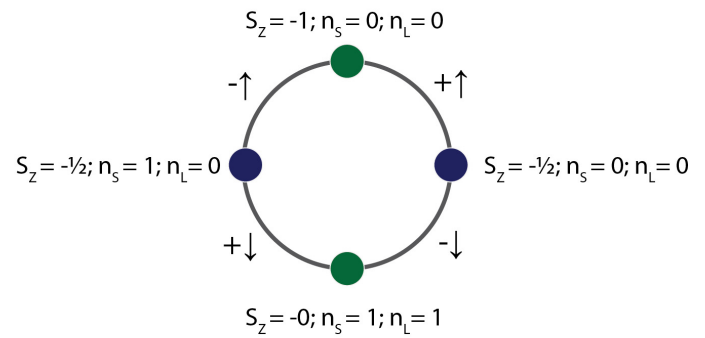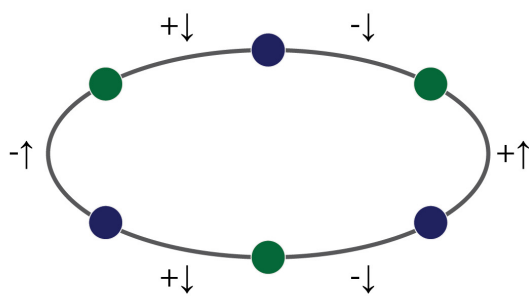
(a) All possible 4-cycles based on single-electron tunneling events
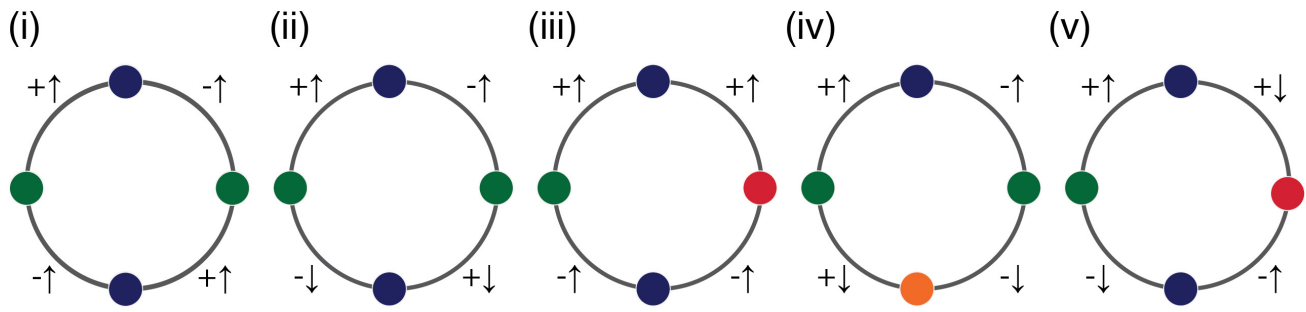
(b) An example valid 6-cycle for the single-particle model

(c) An example valid 4-cycle for the effective model

● : N   ● : N+1   ● : N+2   ● : N-1

FIG. 6. Enumeration of cycles. (a) All possible 4-cycles that involve two electrons tunneling into and two electrons tunneling out of an antidot are shown in schematics (i)–(v). The color of the nodes indicates the number of electrons in the antidot following the schematics in the clockwise direction; counter-clockwise cycle node labeling is given by changing the sign of the added or subtracted electrons (e.g., $N + 1$ in the clockwise labeling becomes $N − 1$ in the counter-clockwise labeling). (b) An example of a 6-cycle demonstrating a pattern of electrons tunneling into and out of the antidot that does not invalidate any of the energy or spin conservation rules for the single-particle antidot model. (c) An example of a valid 4-cycle for the effective model with the full quantum numbers labeled for each state. Notice that this cycle is the same as the one shown in subpanel **A(ii)**.

constraints [see Fig. 6(b)]. First, energy conservation allows the antidot to contain only N and $N+1$ electrons, eliminating the cycles shown in Figs. 6(a)(iii)–6(a)(v). Note that this constraint also applies to the effective model. Second, an individual electron cannot be added and removed (or removed and added) sequentially, since in the network representation, such a process would constitute two nodes connected by an edge rather than a path through a cycle. This second constraint eliminates the cycles shown in Figs. 6(a)(i) and 6(a)(ii) for the single-particle model. This constraint does not apply to the effective model in which electrons are indistinguishable. More precisely, there is no issue in adding or removing the *same* electron since the internal antidot configuration does not track individual electrons, and therefore these 4-cycles are present in networks constructed using the effective model. An example of such a 4-cycle for the effective model is shown in Fig. 6(c).

C. Spin-conserving relaxation effects introduce odd-length cycles

As described in Sec. II E, both the single-particle model and the effective model can incorporate spin-conserving

relaxation effects by adding block matrices to the diagonal of the matrix describing selection rules between eigenstates. For the networks constructed from models that include spin-conserving relaxation effects, an edge represents either a sequential tunneling event or a relaxation event. Including spin-conserving relaxation effects results in a greater number of edges compared with networks excluding relaxation effects corresponding to the same voltage settings (see Fig. S4 in the Supplemental Material), since two nodes may be connected through a spin-conserving relaxation event. Relaxation events do not suppress sequential tunneling events so long as the sequential tunneling rate is on the same order as (or faster than) the relaxation rate; when the relaxation rate is much faster than the tunneling rate, the antidot will effectively remain in its ground state [18]. These relaxation pathways, however, violate the constraints needed to produce a bipartite structure; nodes connected by a relaxation event have the same total spin, so the two-color marking scheme of integer versus half-integer spins discussed in Sec. III B no longer holds.

When we introduce spin-conserving relaxation effects to both models of quantum transport, we observe odd-length
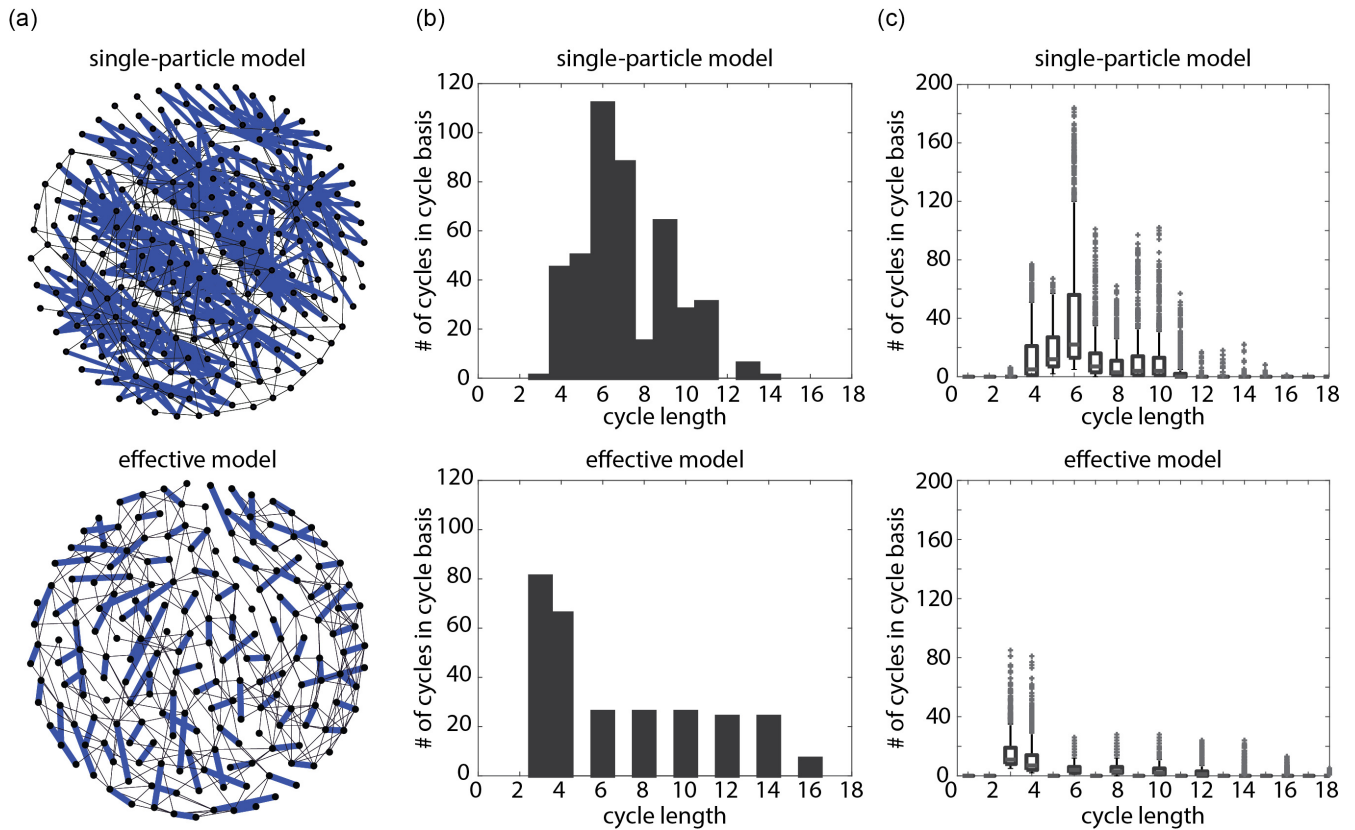
FIG. 7. Spin-conserving relaxation effects introduce odd-length cycles. (a) Example networks with edges corresponding to spin-conserving relaxations highlighted in blue for the single-particle model (top) and the effective model (bottom). (b) Cycle length distribution for the single networks shown in panel (a). (c) Distribution of cycle lengths for all networks over the voltage space displayed in Fig. 2 corresponding to a current greater than 1 pA for the networks constructed from the single-particle model (top) and the effective model (bottom). In each box plot, the central mark represents the median, the top and bottom edges indicate the third and first quartiles, the whiskers extend to $\pm 2.7\sigma$, and individual outliers are displayed by –.

cycles; yet it is important to note that the models' distinct mechanisms of spin-conserving relaxation alter the network structures in different ways [Fig. 7(a)]. For the single-particle model, a relaxation between antidot configurations i and j is allowed if configuration j results from moving one of the electrons in configuration i to the lowest available orbital in configuration i. Since there are multiple possible excited configurations accessible for a given number of electrons, a ground configuration node has multiple edges corresponding to relaxations from different possible excited states [Fig. 7(a)]. As a result, cycles can contain multiple relaxations; cycle basis elements containing an odd number of relaxations result in odd-length cycles in the cycle basis distribution, whereas cycle basis elements containing an even number of relaxations result in even-length cycles [Figs. 7(b) and 7(c)].

For the effective model, a relaxation between states i and j is allowed if both configurations have the same number of particles N and the same spin-excitation quantum number nS, and if the density spin excitation number of configuration j is less than the density spin excitation number of configuration i. Since the only possible density spin excitation numbers are 0 and 1, each node has at most one edge corresponding to a spin-conserving relaxation [Fig. 7(a)]. This fact is reflected in the only odd-length cycles in the cycle basis of the effective model as 3-length cycles, since there is at most one relaxation

in a cycle basis element [Figs. 7(b) and 7(c)]. In sum, while including spin-conserving relaxation effects results in odd-length elements in the cycle basis for networks constructed using both the single-particle and effective models, the models' distinct mechanisms to describe excitations yield different cycle structures.

D. Degree distribution

While cycles are a higher-order topological characteristic that describes the organization of edges which are more than one hop away from a given node, degree distribution is a lower-order topological characteristic that concerns the organization of edges directly connected to a given node. While we observed that distinguishability of particles and different mechanisms for relaxation impact the cycle structure of the networks, we seek to understand how the different physical representations of the antidot impact network structure locally. Degree distribution is one of the most fundamental properties of a network used to discern well-known types of networks, such as scale-free networks, Erdős-Rényi random graphs, and lattices, and is particularly relevant for questions pertaining to controlling many-body quantum systems with applications in quantum information processing devices, since the distribution of edges in a network governs how
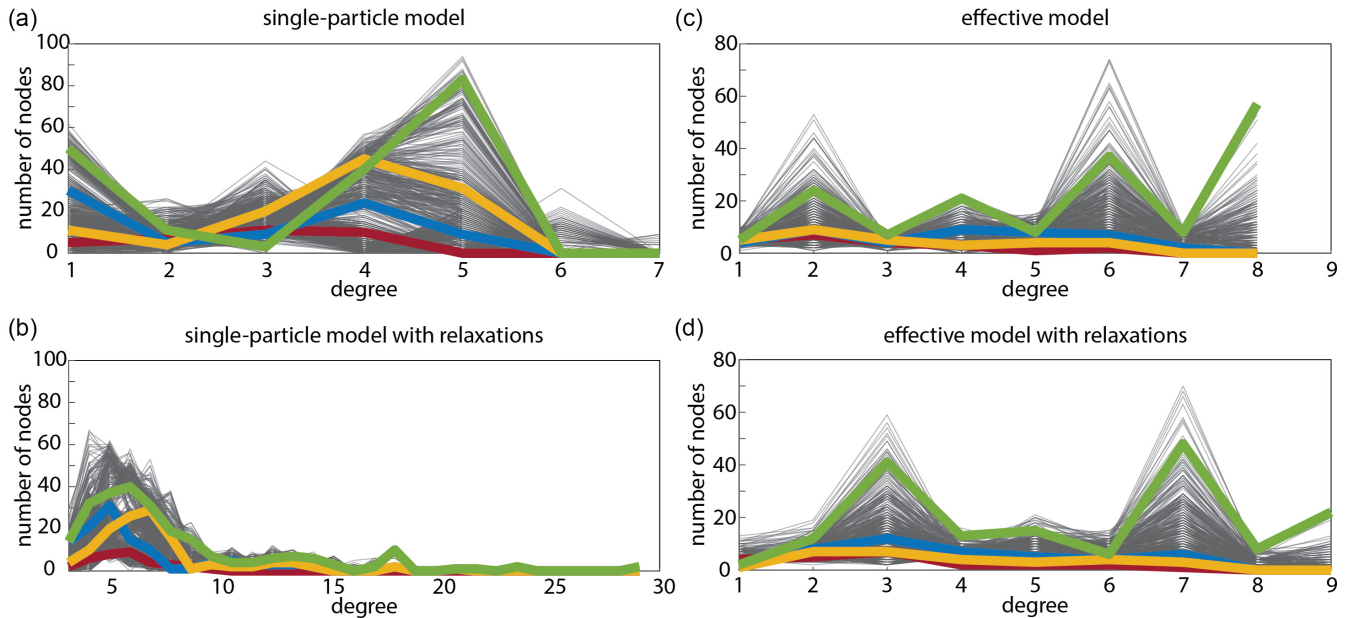
FIG. 8. Physical constraints limit the tail of the degree distribution. The degree distribution of networks constructed using the (a) single-particle model, (b) single-particle model with spin-conserving relaxation effects, (c) effective model, and (d) effective model with spin-conserving relaxation effects. Each network corresponds to voltage settings resulting in $|I| > 1\,\mathrm{pA}$. Networks corresponding to the 25, 50, and 75 percentile values and the maximum value of current over the voltage regime examined are highlighted in red, blue, yellow, and green in panels (a) and (c). The networks corresponding to the same voltage settings in (b) as in (a) and in (d) as in (c) are highlighted in the corresponding color.

information flows locally from one node to another [61,62]. More broadly, we are also interested in how the degree distribution of state-transition networks using two different models of internal antidot configurations compares with other naturally occurring networks.

Unlike many other social, biological, and physical networks, the quantum transport networks studied here do not exhibit a strongly heavy-tailed degree distribution, nor one following a power law or exponentially truncated power law. This fact is true regardless of which underlying physical model was used to construct the networks and whether spin-conserving relaxation effects were included (see Fig. 8) [63]. The longest tail observed was for the single-particle model with relaxation. For both models, quantum mechanical selection rules govern how many energy states are accessible from a given energy state, so there is a physical constraint on the maximum number of edges connected to a single node. While the physical constraints on the number of edges limits the length of the distribution's tail, we observe that the degree distributions do not display any scaling behavior (broad scale, scale-free, or single-scale) before the cutoff [64]. Moreover, the distributions are not unimodal, bimodal, or, in general, smooth.

Relaxation effects alter edges within a network, so incorporating spin-conserving relaxation effects alters the degree distribution of the network (see Fig. 8). In the effective model, adding spin-conserving relaxation effects results in at most one additional edge for each node; given an antidot configuration with an excited density mode, there is only one possible relaxation to a state with the same total spin and spin excitation but with no density mode. We observe the introduction of spin-conserving relaxations in the effective

model as a shift in peaks of the degree distribution between models with and without relaxation [see Figs. 8(c) and 8(d). In the single-particle model, there are multiple possible excited antidot configurations that will relax to the same ground configuration, so including spin-conserving relaxation effects can yield more than one additional edge for a single node. The maximum number of observed edges due to relaxation effects for a single node was 24. We observe the introduction of spin-conserving relaxation effects for the single-particle model through the lengthened tail of the degree distribution [see Figs. 8(a) and 8(b)], whereas we observe the introduction of spin-conserving relaxation effects for the effective model as a shift in peaks from even- to odd-degrees in the degree distribution [see Figs. 8(c) and 8(d)]. Altogether, we observed that spin conservation, particle distinguishability, selection rules, and relaxation mechanisms shape both lower- and higher-order topological characteristics of state-transition networks with implications for the dynamical properties and control profiles of quantum transport networks.

E. Null models demonstrate the impact of dynamics on network structure

Although we motivate our study of the higher- and lower-order topological characteristics of networks representing two different models of antidot transport systems from the observation that the dynamic behaviors of the networks are qualitatively different (Fig. 3), we turn back to examine how the dynamics of the antidot transport system drives the network topology. We do so by examining how the average dynamic cycle length for classical random walkers on the transition state matrices changes with null model experiments.
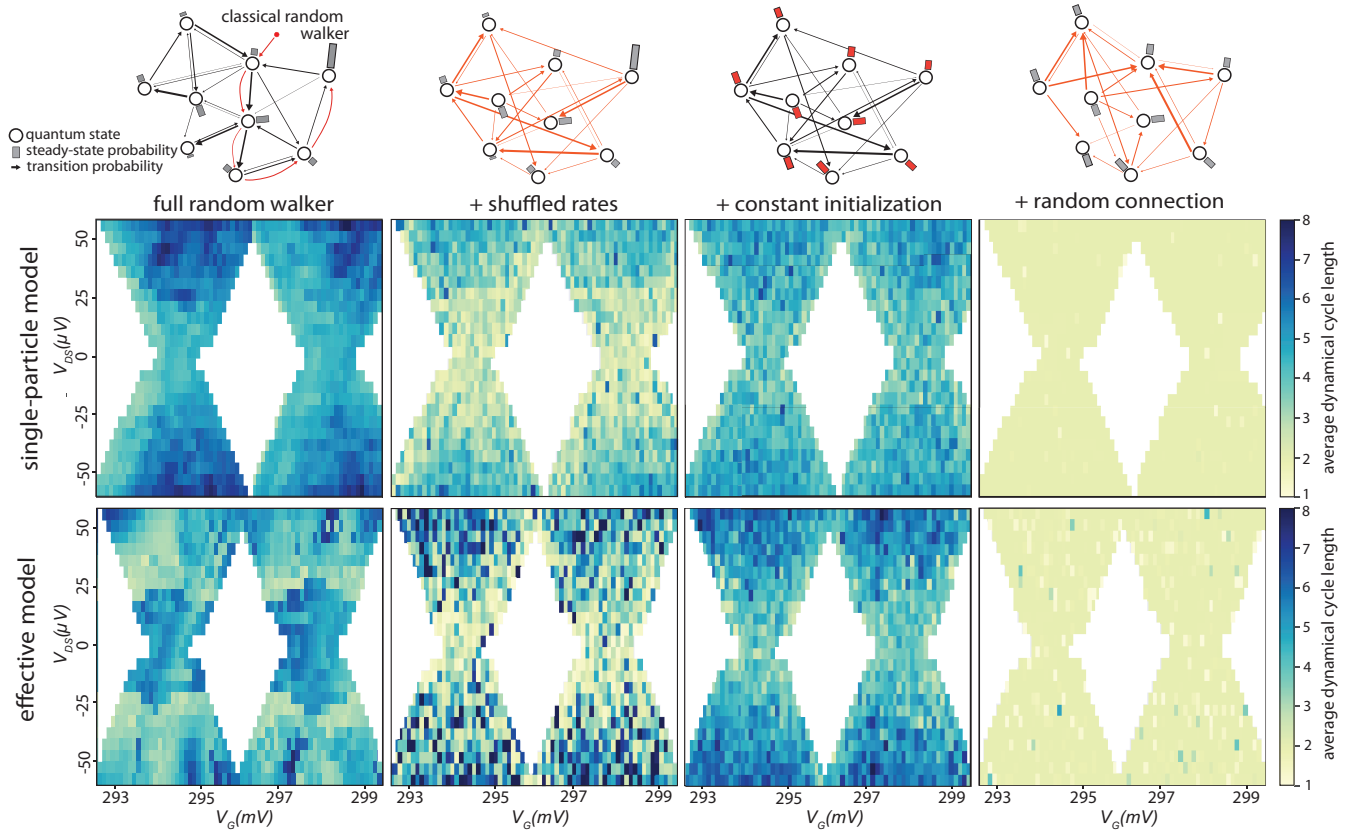
FIG. 9. Steady-state occupation probabilities and transition rates drive dynamic network topology. Average dynamic cycle length is displayed for (top) the single-particle model and (bottom) the effective model when 10 000 classical random walkers after 10 000 times steps are, from left to right: (full random walker) initialized via the steady-state probability weights and evolved forward based on the original transition rate matrices; (shuffled rates) initialized via the steady-state probability weights and evolved forward based on transition rate matrices with conserved connectivity but shuffled transition rates; (constant initialization) initialized randomly via a uniform probability distribution and evolved forward based on the original transition rate matrices; and (random connection) initialized via the steady-state probability weights and evolved forward based on transition rate matrices with the connectivity reshuffled randomly.

In Fig. 9, where the random walkers are initialized via the steady-state occupation vector and the system is evolved forward via the transition rate matrices, we observe a similar qualitative difference in average dynamic cycle length between the single-particle model and the effective model as observed in the diffusion study in Sec. III A. That is, the networks constructed using the effective model display discontinuous transitions between values of average dynamic cycle length within the voltage space, whereas we observe a comparatively more continuous transition between values of average dynamic cycle length for the single-particle model.

For all null model experiments performed, we found that this distinctive qualitative difference regarding continuity of transitions between values of average dynamic cycle length within the voltage space across the single-particle and effective models disappears (Fig. 9). Furthermore, we found that for all null model experiments, both voltage spaces display patterns of average cycle length that are qualitatively similar to each other, but qualitatively different from either of the full random walker simulations. This observation supports our hypothesis that the transport dynamics drive the topological structure and network dynamics of the energy-state networks.

In the shuffled rates and constant initialization null experiments, both of which preserve connectivity within the

transition rate matrices but alter the relative weighting of the initial distribution of walkers or the relative weights of transitions across edges, the voltage space loses much of the structure of average cycle length observed in the full random walker simulations for both null model experiments. That is, the values of the initial steady-state distribution combined with the transition rates drive the qualitative features of the landscape of dynamic network features.

In the random connection experiments, we observe that shuffling the transition rates among the energy states quantitatively shortens the average dynamic cycle lengths for both the single-particle and the effective models. Reshuffling the edges preserved the single connected component, so walkers were not isolated in small, unreachable connected components. Rather, the shuffled dynamics prevented the walkers from traveling within the network. This observation indicates that the connectivity of edges embedded in the transition rate dynamics drives the propagation of information throughout the network.

Taken together, these null model simulations enable us to connect the dynamics of the antidot transport system with the network topologies of the different models we use to study the physics of the system. In particular, the steady-state occupation probabilities and values of transition rates appear

to drive the differences in qualitative dynamic behaviors such as average dynamic cycle length we observe across the two systems; evidence for this relation arises from the fact that when we remove this feature from the simulations, the behavior within the voltage space of continuity between values of average dynamic cycle length is qualitatively similar. Furthermore, the connectivity, or underlying network structure, of the transition rates themselves appears to be the primary driver of the lengths of the dynamic cycles; evidence for this relation arises from the fact that shuffling the connectivity of the transition rate matrices leads to the walkers exhibiting excitatory rather than cyclic behavior.

IV. DISCUSSION

A. Effective models of many-body quantum systems

Many-body quantum systems are difficult to simulate on classical computing systems because the number of parameters necessary to represent the system grows exponentially with particle number. As a result, physicists have devised effective models that can be implemented numerically to describe many-body quantum systems. In using effective models, physicists make explicit decisions about how to describe a system as well as which physical effects to include, depending on the question they seek to answer [65]. In the many-body quantum system studied here, chiral edge waves of the quantum antidot in a two-dimensional electron gas system can be viewed either in terms of the electron state occupation numbers (as in the single-particle model) or as edge waves in the charge distribution (as in the effective model) [36]. Both models are useful; they yield quantitative values for current and conductance that match experimental data and also recreate many qualitative features of transport experiments. These two models are even connected through the maximum-density-droplet state, in which the ground eigenstate of the single-particle model is exactly the ground-state solution to the many-particle Hamiltonian, even when accounting for electron-electron interactions [37].

While the two models studied here both yield values of current and conductance in agreement with time-averaged experimental data, they describe different mechanisms for transport. In the single-particle model, distinguishable electrons tunnel to discrete antidot states labeled by occupation vectors, and individual electrons occupy excited states. In the effective model, indistinguishable electrons tunnel to discrete antidot states labeled by collective spin and density modes. While the difference in how these antidot states are labeled does not impact time-averaged values for current and conductance, our results demonstrate that the choice of underlying physical model impacts the nature of state transitions allowed, which in turn defines the collective energy landscape on which the system exists. These dependencies manifest in two fundamental aspects of the state transition network's structure: the degree distribution and the cycle structure.

Given the growing interest in network-based approaches to study, model, and control systems governed by quantum physics, our network-based approach to study transport through quantum antidots represents a paradigm to begin to move toward network-based control strategies [46,66–68].

By finding similarities across networks constructed to represent the same system but using different underlying models, we can better understand which network characteristics reflect physical constraints versus the mechanisms of a specific model. For example, as reported in Sec. III B, networks representing antidot systems without spin-conserving relaxation effects are bipartite, regardless of which model was used to represent antidot states. This result indicates that control-based strategies designed specifically for bipartite networks may be appropriate to manipulate the antidot to a desired state in regimes in which spin-conserving relaxation effects do not play a role [69]. Altogether, the network-based approach presented here illuminates how different mechanisms to describe transport have different implications for the dynamics and control of many-body quantum systems.

B. Cycle structure and degree distribution in quantum transport networks

The ability to control many-body quantum systems has become increasingly important in quantum information processing devices. The ability to identify driver nodes, devise control strategies, and design robust (un)controllable subsystems is crucial in order to store, encode, process, and protect information across biological, technological, and quantum systems [5,70–72]. Controlling transport is key to many quantum technologies, and both the cycle structure and the degree distribution impact the control profiles of complex networks [34]. A network's control profile comprises its response to various perturbations designed to guide the system towards specific states. One metric commonly used to evaluate this response is the network's controllability. A network is controllable if we can identify a set of inputs or driver nodes such that the network can be driven from any initial condition to a target condition within a finite amount of time. The degree distribution of a network has a large role in determining the number of driver nodes in the control profile of a network, where driver nodes tend to avoid high-degree nodes [73]. More generally, the degree distribution dictates how a control signal propagates to neighboring nodes, and cycles dictate how those control signals reverberate in feedback loops. Designing efficient control strategies for complex networks therefore requires an understanding and accounting of both the degree distribution and cycle structure.

To better understand the role of cycle structure in the available dynamics, as well as their control, it is useful to consider the study of cycles in real-world systems. Recent work examining the cycle structure of biological, physical, and engineered systems has shown that cycle structure impacts information propagation, information storage, feedback, resilience to noise, and robustness [32,33,74–76]. Robustness of a network refers to the ability of a network to continue carrying out a given function when a fraction of its components is damaged. By definition, cycles increase the robustness of transport in a network under an attack that breaks edges, and dense cycle structures have been shown to optimize transport function in response to varying loads and resilience to damage in biological systems such as leaf vasculature and insect wing veins, engineered systems such as city streets, and physical networks such as river deltas [55]. While a tree structure is

optimal for transport when there is a spatially and temporally constant load, optimization under varying loads and robustness to an attack dictates the opposite of a treelike structure [77,78]. Robustness of transport to an edge attack requires that breaking any one edge does not yield a disconnected network, and while the optimal structure for a network at any single point in time may be treelike, the overall optimization of spatially and temporally varying transport load requires redundant paths in the form of cycles. Furthermore, cycles play a role in the dynamic stability (the tendency of a network to return to an equilibrium state after a perturbative disturbance) of biological and engineered networks [79]. For example, long cycles are relevant to maintain excitable dynamics in neural networks [51] and short cycles are responsible for maintaining sustained activity [50]. Dynamic states in networks with longer cycles persist for a longer period of time than those with shorter cycles [80]. Cycle structure can also influence mechanical properties of physical systems. For example, recent work has shown that short cycles in polymer networks influence rubber elasticity [81]. Collectively, these studies underscore the key role of cycle structure in a network's dynamics and function.

Complementing a network's cycle structure is its degree distribution. A network's degree distribution impacts the dynamics whereby information flows and is distributed throughout a network, as well as the network's controllability and robustness to damage. Dynamically, networks dominated by either even- or odd-degree nodes have different properties: networks dominated by odd-degree nodes tend to noise-induced energy-state changes more than those dominated by even-degree nodes [80]. Networks with a large fraction of odd-degree nodes have been shown to have more unstable dynamics compared with networks with a higher fraction of even-degree nodes. The reason is intuitive: nodes with an odd degree always have an unpaired edge, leaving the network more susceptible to dynamically unstable (chaotic) behavior since unpaired edges can cause a network to tend toward getting stuck in certain states [80]. The degree distribution is also an important topological feature in understanding how robust a network is to both random and targeted attacks, such as an attack in which edges connected to the highest degree nodes are targeted for removal. For example, a bimodal degree distribution optimizes network robustness in the face of both random and targeted attacks [82]. Collectively, these studies underscore the fundamental relevance of the degree distribution for a network's dynamics.

It is interesting to consider our results in light of this extensive literature. Specifically, recall we found that altering the physical model underlying the description of internal antidot configurations impacts both the degree distribution and cycle structure of network representations. The network structures have different implications for the dynamical properties and control profiles of the antidot system. For example, for the networks constructed using the effective model without spin-conserving relaxation effects, the networks are dominated by even-degree nodes, whereas when spin-conserving relaxation effects are included, the networks are dominated by odd-degree nodes [see Figs. 8(c) and 8(d)]. On a dynamical level, this shift from the relative prevalence of even- versus odd-degree nodes indicates that spin-conserving relaxation effects

may serve a destabilizing role in the networks. In terms of network robustness, while the shortest path between two nodes is the most efficient route to communicate information between them, it may not be the optimal route when taking into account traffic, noise, and resistance. In the case of the transport networks, barriers preventing the shortest path between two nodes from being the optimal include passing through an antidot configuration that is energetically costly or improbable to reach (for a discussion of such barriers in the state space, and their relevance for control, see Ref. [68]). In this case, information may flow through paths that are not topologically the shortest, and hence short cycles are critical to provide alternative paths and to improve fault tolerance [75]. We found that in models excluding spin-conserving relaxation effects, the shortest cycle basis elements differ based on whether internal antidot configurations are represented using occupation vectors (as in the single-particle model) or collective spin and density modes (as in the effective model) (see Fig. 5). Our results indicate that altering the underlying representation of nonequilibrium transport through quantum antidots has profound implications for understanding the dynamics and devising control strategies for many-body quantum systems.

C. Methodological limitations and future directions

Several methodological considerations are pertinent to this paper. First, we compared the structure of quantum transport networks constructed using two underlying models of internal antidot configurations: a single-particle model and an effective model. The implementation of sequential transport used for both models does not include higher-order cotunneling processes or spin-flip relaxation effects (due to hyperfine coupling or phonon-mediated spin-orbit interactions [18]), both of which may be present in experiments. Yet, even without including these effects, we find close quantitative agreement between the computational model and experiments [31]. Notably, our approach does allow spin-flip relaxation effects to be incorporated by adding block transition matrices between elements off the main diagonal of Eq. (5).

Second, while the undirected networks allow us to probe the relationship between topology and quantum networks at the most fundamental level, certain physical effects that may impact dynamics are buried. For example, in the undirected networks, both tunneling events and relaxations are represented as undirected edges, when relaxations may be more accurately represented as directed edges. A natural extension of this paper would be to explore the network properties of directed networks with edges weighted by occupation probabilities and transition rates.

Third, since enumerating all of the cycles in a network is a computationally intensive process that typically employs a brute-force depth-first search algorithm [83], we explore the cycle basis to probe basic features of the cycle structure. While there may be many cycle bases corresponding to a cycle space, the lengths of the cycle basis elements are fixed, so the analysis of length of elements in the cycle bases does not depend on the choice of basis. Future work could further explore the cycle structure of these networks by examining the first Betti number [84,85], characterizing loop redundancy

[86,87], and by using other statistical measures to characterize the number of cycles [88].

Fourth, our findings directly motivate experiments to probe the dynamics of quantum transport. For example, full counting statistics experiments directly measure tunneling rates and the distribution function of current fluctuations by measuring individual electron tunneling events [89]. Our numerical simulations of antidot transport could be expanded to yield electron counting statistics and current correlation functions resolved by spin and edge states, which would enable us to more directly study the dynamical properties of transport. The current correlation functions would be directly related to the dynamical transitions of the system between different internal states. Comparisons of these dynamical properties between effective models, and with experimental data, could further elucidate the role of network topology on system dynamics, and help to differentiate between physical models that are not easily distinguishable based on current and conductance measurements alone.

Finally, the framework of constructing and analyzing networks developed here generalizes to any system that can be modeled as a Markov process. Markovian processes are often sufficient to capture the effects of stochastic processes in interactions between a discrete quantum system and an infinite bath. Some examples are cavity-QED experiments [90], superconducting qubit systems [91], trapped-ion systems [92], and generic quantum computers under broadband control [93]. Optically driven quantum systems are another interesting example of a Markovian process, where transitions between internal quantum states involve the absorption or emission of single photons. As for the electronic transport system we study in this paper, different models of the internal dynamics can yield identical predictions for the steady-state photon emission rate, whereas dynamical information appearing in the correlation function of emitted photons can be used to distinguish between models [94].

As the complexity of experimentally accessible quantum systems increases beyond the point at which exact calculations are tractable, alternative methods to assess and classify their dynamics are urgently required. Here we draw attention to lengths of cycles in the cycle basis and degree distribution as two network characteristics of particular interest for their ability to reflect fundamental mechanisms specific to different physical models as well as for their relevance in understanding system dynamics and implications for devising control strategies. Our paper represents a general framework to analyze different models of many-body quantum systems using a network-science approach as an example of the ways in which concepts from classical network science can address pressing challenges in quantum information science.

V. CONCLUSION

Using network science to study the energy-state transitions of nonequilibrium transport through a quantum antidot based on two different models of internal antidot states, we demonstrated that structural properties of the network reflect model-specific spin and energy constraints. These constraints result in different minimum-length elements in the cycle bases across models as well as different degree distributions. This understanding of how different physical models of mesoscopic quantum phenomena alters network structure may inform the design and control of quantum devices for quantum simulation, storage, or information processing.

[1] J. Biamonte, M. Faccin, and M. De Domenico, Complex networks from classical to quantum, Commun. Phys. **2**, 53 (2019).

[2] G. Bianconi, Interdisciplinary and physics challenges of network theory, Europhys. Lett. **111**, 56001 (2015).

[3] M. A. Lohe, Quantum synchronization over quantum networks, J. Phys. A: Math. Theor. **43**, 465301 (2010).

[4] O. Mülken, M. Dolgushev, and M. Galiceanu, Complex quantum networks: From universal breakdown to optimal transport, Phys. Rev. E **93**, 022304 (2016).

[5] A. Cabot, F. Galve, V. M. Eguíluz, K. Klemm, S. Maniscalco, and R. Zambrini, Unveiling noiseless clusters in complex quantum networks, npj Quantum Inf. **4**, 57 (2018).

[6] S. Chakraborty, L. Novo, A. Ambainis, and Y. Omar, Spatial Search by Quantum Walk is Optimal for Almost all Graphs, Phys. Rev. Lett. **116**, 100501 (2016).

[7] R. Kumar, S. Kumari, and M. Bala, Quantum mechanical model of information sharing in social networks, Soc. Network Anal. Min. **11**, 1 (2021).

[8] C. F. Negre, H. Ushijima-Mwesigwa, and S. M. Mniszewski, Detecting multiple communities using quantum annealing on the *d*-wave system, PLoS One **15**, e0227538 (2020).

[9] S. M. Mniszewski, P. A. Dub, S. Tretiak, P. M. Anisimov, Y. Zhang, and C. F. Negre, Reduction of the molecular hamiltonian matrix using quantum community detection, Sci. Rep. **11**, 4099 (2021).

[10] J. I. Cirac, P. Zoller, H. J. Kimble, and H. Mabuchi, Quantum State Transfer and Entanglement Distribution Among Distant Nodes in a Quantum Network, Phys. Rev. Lett. **78**, 3221 (1997).

[11] A. N. Poteshman, E. Tang, L. Papadopoulos, D. S. Bassett, and L. C. Bassett, Network architecture of energy landscapes in mesoscopic quantum systems, New J. Phys. **21**, 123049 (2019).

[12] D. Loss and D. P. DiVincenzo, Quantum computation with quantum dots, Phys. Rev. A **57**, 120 (1998).

[13] D. D. Awschalom, L. C. Bassett, A. S. Dzurak, E. L. Hu, and J. R. Petta, Quantum spintronics: Engineering and manipulating atom-like spins in semiconductors, Science **339**, 1174 (2013).

[14] P. Barthelemy and L. M. Vandersypen, Quantum dot systems: A versatile platform for quantum simulations, Ann. Phys. **525**, 808 (2013).

[15] S. E. Economou, J. I. Climente, A. Badolato, A. S. Bracker, D. Gammon, and M. F. Doty, Scalable qubit architecture based on holes in quantum dot molecules, Phys. Rev. B **86**, 085319 (2012).

[16] L. P. Kouwenhoven, G. Schön, and L. L. Sohn, Introduction to mesoscopic electron transport, in *Mesoscopic Electron Transport*, edited by L. L. Sohn, L. P. Kouwenhoven, and G. Schön, NATO ASI Series, Vol. 345 (Springer, Dordrecht, 1997), pp. 1–44

[17] W. G. van der Wiel, S. De Franceschi, J. M. Elzerman, T. Fujisawa, S. Tarucha, and L. P. Kouwenhoven, Electron transport through double quantum dots, Rev. Mod. Phys. **75**, 1 (2002).

[18] R. Hanson, L. P. Kouwenhoven, J. R. Petta, S. Tarucha, and L. M. K. Vandersypen, Spins in few-electron quantum dots, Rev. Mod. Phys. **79**, 1217 (2007).

[19] H.-S. Sim, M. Kataoka, and C. J. Ford, Electron interactions in an antidot in the integer quantum Hall regime, Phys. Rep. **456**, 127 (2008).

[20] P. Tighineanu, A. S. Sørensen, S. Stobbe, and P. Lodahl, Unraveling the Mesoscopic Character of Quantum Dots in Nanophotonics, Phys. Rev. Lett. **114**, 247401 (2015).

[21] C.-J. Yang and J.-H. An, Resonance fluorescence beyond the dipole approximation of a quantum dot in a plasmonic nanostructure, Phys. Rev. A **93**, 053803 (2016).

[22] A. A. Bagrov, M. Danilov, S. Brener, M. Harland, A. I. Lichtenstein, and M. I. Katsnelson, Detecting quantum critical points in the $t - t'$ Fermi-Hubbard model via complex network theory, Sci. Rep. **10**, 20470 (2020).

[23] M. A. Valdez, D. Jaschke, D. L. Vargas, and L. D. Carr, Quantifying Complexity in Quantum Phase Transitions via Mutual Information Complex Networks, Phys. Rev. Lett. **119**, 225301 (2017).

[24] B. Sundar, M. A. Valdez, L. D. Carr, and K. R. A. Hazzard, Complex-network description of thermal quantum states in the Ising spin chain, Phys. Rev. A **97**, 052320 (2018).

[25] S. Zaman and W.-C. Lee, Real-space visualization of quantum phase transitions by network topology, Phys. Rev. E **100**, 012304 (2019).

[26] M. Walschaers, B. Sundar, N. Treps, L. D. Carr, and V. Parigi, Emergent complex quantum networks in continuous-variables non-Gaussian states, Quantum Sci. Technol. **8**, 035009 (2023).

[27] D. Andrieux and P. Gaspard, Fluctuation theorem for transport in mesoscopic systems, J. Stat. Mech.: Theory Exp. (2006) P01011.

[28] D. Andrieux and P. Gaspard, Fluctuation theorem for currents and Schnakenberg network theory, J. Stat. Phys. **127**, 107 (2007).

[29] M. Stone, Edge waves in the quantum Hall effect, Ann. Phys. **207**, 38 (1991).

[30] M. Stone, Schur functions, chiral bosons, and the quantum-Hall-effect edge states, Phys. Rev. B **42**, 8399 (1990).

[31] L. C. Bassett, Probing electron-electron interactions with a quantum antidot, Ph.D. thesis, University of Cambridge, 2009.

[32] J. T. Lizier, F. M. Atay, and J. Jost, Information storage, loop motifs, and clustered structure in complex networks, Phys. Rev. E **86**, 026110 (2012).

[33] S. Boccaletti, V. Latora, Y. Moreno, M. Chavez, and D.-U. Hwang, Complex networks: Structure and dynamics, Phys. Rep. **424**, 175 (2006).

[34] C. Campbell, J. Ruths, D. Ruths, K. Shea, and R. Albert, Topological constraints on network control profiles, Sci. Rep. **5**, 18693 (2015).

[35] D. R. Mace, C. H. W. Barnes, G. Faini, D. Mailly, M. Y. Simmons, C. J. B. Ford, and M. Pepper, General picture of quantum Hall transitions in quantum antidots, Phys. Rev. B **52**, R8672 (1995).

[36] M. Stone, H. W. Wyld, and R. L. Schult, Edge waves in the quantum Hall effect and quantum dots, Phys. Rev. B **45**, 14156 (1992).

[37] A. H. MacDonald, S. E. Yang, and M. D. Johnson, Quantum dots in strong magnetic fields: Stability criteria for the maximum density droplet, Aust. J. Phys. **46**, 345 (1993).

[38] N. W. Ashcroft and N. D. Mermin, *Solid State Physics* (Brooks/Cole, Belmont, CA, 1976).

[39] See Supplemental Material at http://link.aps.org/supplemental/10.1103/PhysRevResearch.5.023125 for additional methodological details and supplementary results.

[40] J. M. Luttinger, An exactly soluble model of a many-fermion system, J. Math. Phys. **4**, 1154 (1963).

[41] S. Tomonaga, Remarks on Bloch's method of sound waves applied to many-fermion problems, Prog. Theor. Phys. **5**, 544 (1950).

[42] M. Mitchell, *Complexity: A Guided Tour* (Oxford University Press, New York, NY, 2011).

[43] M. Newman, *Networks: An Introduction* (Oxford University Press, New York, NY, 2010).

[44] R. Albert and A.-L. Barabási, Statistical mechanics of complex networks, Rev. Mod. Phys. **74**, 47 (2002).

[45] C. W. Lynn, L. Papadopoulos, A. E. Kahn, and D. S. Bassett, Human information processing in complex networks, Nat. Phys. **16**, 965 (2020).

[46] J. Z. Kim, J. M. Soffer, A. E. Kahn, J. M. Vettel, F. Pasqualetti, and D. S. Bassett, Role of graph architecture in controlling dynamical networks with applications to neural systems, Nat. Phys. **14**, 91 (2018).

[47] D. M. Lydon-Staley, D. Zhou, A. S. Blevins, P. Zurn, and D. S. Bassett, Hunters, busybodies and the knowledge network building associated with deprivation curiosity, Nat. Hum. Behav. **5**, 327 (2021).

[48] A. E. Sizemore, E. A. Karuza, C. Giusti, and D. S. Bassett, Knowledge gaps in the early growth of semantic feature networks, Nat. Hum. Behav. **2**, 682 (2018).

[49] A. E. Sizemore, C. Giusti, A. Kahn, J. M. Vettel, R. F. Betzel, and D. S. Bassett, Cliques and cavities in the human connectome, J. Comput. Neurosci. **44**, 115 (2018).

[50] G. C. Garcia, A. Lesne, M.-T. Hütt, and C. C. Hilgetag, Building blocks of self-sustained activity in a simple deterministic model of excitable neural networks, Front. Comput. Neurosci. **6**, 50 (2012).

[51] G. C. Garcia, A. Lesne, C. C. Hilgetag, and M.-T. Hütt, Role of long cycles in excitable dynamics on graphs, Phys. Rev. E **90**, 052805 (2014).

[52] G. Bianconi and A. Capocci, Number of Loops of Size h in Growing Scale-Free Networks, Phys. Rev. Lett. **90**, 078701 (2003).

[53] A. Hagberg, P. Swart, and D. S Chult, Exploring network structure, dynamics, and function using NetworkX, Tech. Rep. (Los Alamos National Lab. (LANL), Los Alamos, NM, 2008).

[54] K. Paton, An algorithm for finding a fundamental set of cycles of a graph, Commun. ACM **12**, 514 (1969).

[55] E. Katifori, G. J. Szöllősi, and M. O. Magnasco, Damage and Fluctuations Induce Loops in Optimal Transport Networks, Phys. Rev. Lett. **104**, 048704 (2010).

[56] T. Gavrilchenko and E. Katifori, Resilience in hierarchical fluid flow networks, Phys. Rev. E **99**, 012321 (2019).

[57] T. Kavitha, C. Liebchen, K. Mehlhorn, D. Michail, R. Rizzi, T. Ueckerdt, and K. A. Zweig, Cycle bases in graphs characterization, algorithms, complexity, and applications, Comp. Sci. rev. **3**, 199 (2009).

[58] M. Safar, K. Alenzi, and S. Albehairy, Counting cycles in an undirected graph using DFS-XOR algorithm, in *2009 First International Conference on Networked Digital Technologies, Ostrava, Czech Republic* (IEEE, 2009), pp. 132–139.

[59] A. Mikalčiūtė and L. Vilčiauskas, Insights into the hydrogen bond network topology of phosphoric acid and water systems, Phys. Chem. Chem. Phys. **23**, 6213 (2021).

[60] J.-L. Guillaume and M. Latapy, Bipartite structure of all complex networks, Inform. Process. Lett. **90**, 215 (2004).

[61] M. E. J. Newman, S. H. Strogatz, and D. J. Watts, Random graphs with arbitrary degree distributions and their applications, Phys. Rev. E **64**, 026118 (2001).

[62] K. Bogner, M. Müller, and M. P. Schlaile, Knowledge diffusion in formal networks: The roles of degree distribution and cognitive distance, Int. J. Comput. Econ. Econometrics **8**, 388 (2018).

[63] A.-L. Barabási and E. Bonabeau, Scale-free networks, Sci. Am. **288**, 60 (2003).

[64] L. A. Amaral, A. Scala, M. Barthelemy, and H. E. Stanley, Classes of small-world networks, Proc. Natl. Acad. Sci. **97**, 11149 (2000).

[65] G. Galli, The long and winding road: Predicting materials properties through theory and computation, Handb. Mater. Model.: Methods: Theory Model.37 (2020).

[66] G. Baggio, D. S. Bassett, and F. Pasqualetti, Data-driven control of complex networks, Nat. Commun. **12**, 1429 (2021).

[67] J. G. T. Zañudo, G. Yang, and R. Albert, Structure-based control of complex networks with nonlinear dynamics, Proc. Natl. Acad. Sci. **114**, 7234 (2017).

[68] A. E. Motter, Networkcontrology, Chaos **25**, 097621 (2015).

[69] J. C. Nacher and T. Akutsu, Structural controllability of unidirectional bipartite networks, Sci. Rep. **3**, 1647 (2013).

[70] A. J. Daley, Quantum trajectories and open many-body quantum systems, Adv. Phys. **63**, 77 (2014).

[71] V. Ramakrishna and H. Rabitz, Relation between quantum computing and quantum controllability, Phys. Rev. A **54**, 1715 (1996).

[72] J. C. Rozum and R. Albert, Identifying (un)controllable dynamical behavior in complex networks, PLoS Comput. Biol. **14**, e1006630 (2018).

[73] Y.-Y. Liu, J.-J. Slotine, and A.-L. Barabási, Controllability of complex networks, Nature (London) **473**, 167 (2011).

[74] P. G. Lind, M. C. Gonzalez, and H. J. Herrmann, Cycles and clustering in bipartite networks, Phys. Rev. E **72**, 056127 (2005).

[75] X. Zhou, X. Liang, J. Zhao, and S. Zhang, Cycle based network centrality, Sci. Rep. **8**, 11749 (2018).

[76] Y. Yi, Z. Zhang, and S. Patterson, Scale-free loopy structure is resistant to noise in consensus dynamics in complex networks, IEEE Trans. Cybern. **50**, 190 (2020).

[77] S. Bohn and M. O. Magnasco, Structure, Scaling, and Phase Transition in the Optimal Transport Network, Phys. Rev. Lett. **98**, 088702 (2007).

[78] C. Nguyen, D. Peetz, A. E. Elbanna, and J. M. Carlson, Characterization of fracture in topology-optimized bioinspired networks, Phys. Rev. E **100**, 042402 (2019).

[79] A. Ma'ayan, G. A. Cecchi, J. Wagner, A. R. Rao, R. Iyengar, and G. Stolovitzky, Ordered cyclic motifs contribute to dynamic stability in biological and engineered networks, Proc. Natl. Acad. Sci. **105**, 19235 (2008).

[80] F. G. Woodhouse, A. Forrow, J. B. Fawcett, and J. Dunkel, Stochastic cycle selection in active flow networks, Proc. Natl. Acad. Sci. **113**, 8200 (2016).

[81] T. W. Sirk, Growth and arrest of topological cycles in small physical networks, Proc. Natl. Acad. Sci. **117**, 15394 (2020).

[82] T. Tanizawa, G. Paul, R. Cohen, S. Havlin, and H. E. Stanley, Optimization of network robustness to waves of targeted and random attacks, Phys. Rev. E **71**, 047101 (2005).

[83] R. Tarjan, Depth-first search and linear graph algorithms, SIAM J. Comput. **1**, 146 (1972).

[84] M. X. Lim and R. P. Behringer, Topology of force networks in granular media under impact, Europhys. Lett. **120**, 44003 (2017).

[85] A. P. Kartun-Giles and G. Bianconi, Beyond the clustering coefficient: A topological analysis of node neighbourhoods in complex networks, Chaos, Solitons & Fractals: X **1**, 100004 (2019).

[86] A. E. Sizemore, J. E. Phillips-Cremins, R. Ghrist, and D. S. Bassett, The importance of the whole: Topological data analysis for the network neuroscientist, Network Neurosci. **3**, 656 (2019).

[87] A. S. Blevins and D. S. Bassett, Topology in biology, in *Handbook of the Mathematics of the Arts and Sciences*, edited by B. Sriraman (Springer, Cham, 2021), pp. 2073–2095.

[88] G. Bianconi and M. Marsili, Loops of any size and Hamilton cycles in random scale-free networks, J. Stat. Mech.: Theory Exp. (2005) P06005.

[89] S. Gustavsson, R. Leturcq, B. Simovič, R. Schleser, T. Ihn, P. Studerus, K. Ensslin, D. C. Driscoll, and A. C. Gossard, Counting Statistics of Single Electron Transport in a Quantum Dot, Phys. Rev. Lett. **96**, 076605 (2006).

[90] A. Devi, S. D. Gunapala, and M. Premaratne, Coherent and incoherent laser pump on a five-level atom in a strongly coupled cavity-QES system, Phys. Rev. A **105**, 013701 (2022).

[91] S.-l. Ma, J.-k. Xie, and F.-l. Li, Generation of superposition coherent states of microwave fields via dissipation of a superconducting qubit with broken inversion symmetry, Phys. Rev. A **99**, 022302 (2019).

[92] E. Ben Av, Y. Shapira, N. Akerman, and R. Ozeri, Direct reconstruction of the quantum-master-equation dynamics of a trapped-ion qubit, Phys. Rev. A **101**, 062305 (2020).

[93] G. McCauley, B. Cruikshank, S. Santra, and K. Jacobs, Ability of Markovian master equations to model quantum computers and other systems under broadband control, Phys. Rev. Res. **2**, 013049 (2020).

[94] R. E. K. Fishman, R. N. Patel, D. A. Hopper, T.-Y. Huang, and L. C. Bassett, Photon-emission-correlation spectroscopy as an analytical tool for solid-state quantum defects, PRX Quantum **4**, 010202 (2023).